## Coherence of Rabi oscillations with spin exchange

C. Kiehl, \*\* D. Wagner, \*\* T.-W. Hsu, \*\* S. Knappe, \*\*2,3 C. A. Regal, \*\* and T. Thiele\*\*. 

\*\*1JILA, National Institute of Standards and Technology and University of Colorado, and Department of Physics, University of Colorado, Boulder, Colorado 80309, USA 

\*\*2Mechanical Engineering, University of Colorado, Boulder, Colorado 80309, USA 

\*\*3FieldLine Incorporated, Boulder, Colorado 80301, USA



(Received 20 October 2022; accepted 16 December 2022; published 10 January 2023)

Rabi measurements in atomic vapor cells are of current interest in a range of microwave imaging and sensing experiments, but are increasingly in a parameter space outside of theoretical studies of coherence defined by spin-exchange collisions. Here, we study the coherence of Rabi oscillations in vapor cells by employing continuous nondestructive readout of the hyperfine manifold of <sup>87</sup>Rb using Faraday rotation. We develop a full model for spin-exchange coherence for hyperfine transitions that takes into account a nonstatic population distribution. In this regime, Rabi oscillations exhibit nontrivial time-domain signals that allow verification of vapor-cell parameters. We find excellent agreement between theory and experiment, which will aid in benchmarking sensitivities of Rabi measurement applications.

DOI: 10.1103/PhysRevResearch.5.L012002

For sensors based on hot atomic vapors, spin-exchange (SE) collisions are the dominant limitation of sensitivity [1,2]. These collisions originate from the acquired phase shift between singlet and triplet interaction potentials of the electrons of colliding alkali atoms. The exchange interaction conserves the total spin of the colliding atoms, but causes random transitions between the hyperfine ground states that have recently been leveraged in hot atomic vapor cells for generating many-body entanglement [3] and modeling phase transition dynamics [4]. Decoherence effects of SE collisions within a Zeeman manifold have been studied in the context of optically pumped magnetometers (OPMs), and notably even found to disappear in the spin-exchange-relaxation-free (SERF) regime at low magnetic fields [5-7]. Further, the consequences of spin-exchange collisions on the coherence between two hyperfine ground manifolds have also been well studied in the context of masers [8,9] and atomic clocks [1,10]. In these studies, SE decay rates were modeled based on stationary atomic populations such as a spin-temperature (ST) distribution, which is valid when continuous optical pumping and a weak-driving field prevent Rabi oscillations, and SE collisions dominate over other collision and scattering rates. However, this approximation is invalid in the case of a strong driving field, such as a near-resonant microwave field, that causes significant population transfer. As a result, the coherence of

Published by the American Physical Society under the terms of the Creative Commons Attribution 4.0 International license. Further distribution of this work must maintain attribution to the author(s) and the published article's title, journal citation, and DOI.

Rabi oscillations is expected to deviate from the assumptions of weak driving and exhibit nontrivial detuning and spinpolarization dependence.

This picture needs completion, as in the last few years, Rabi oscillations driven within atomic ensembles have been proposed for sensing and imaging microwave fields for applications in characterizing microwave circuits [11–13], self-calibrated vector magnetometry [14], and in medical applications such as cancer detection [15–17]. While microfabricated vapor cells are ideal sensor platforms for these applications due to their compact size and high atomic densities, decoherence is typically dominated by SE collisions when wall collisions are minimized by buffer gas [18]. To unlock new sensitivity regimes for these applications, a complete understanding of the SE coherence is necessary.

In this Letter, we explore the coherence of Rabi oscillations in a heated vapor cell driven on  $\sigma^-$ ,  $\pi$ , and  $\sigma^+$  hyperfine transitions of <sup>87</sup>Rb [Fig. 1(a)] that do not adhere to the weak-driving approximation. By employing continuous quantum nondemolition (QND) measurement readout based on Faraday rotation we are able to study nontrivial time-dependent behavior of the atomic population. Using a full theoretical analysis of SE that accounts for the time-dependent SE dephasing rate caused by population dynamics during Rabi oscillations, we observe excellent agreement between the model and the measured coherence in the continuous Faraday signal.

With this full understanding in hand, we illustrate that the Rabi line shape is connected to many vapor parameters and show that driving multiple transitions can pinpoint useful information. Specifically, we extract from SE coherence consistent values for the vapor temperature, buffer gas pressure, and the atomic state prepared by optical pumping by using the fact that the Rabi envelope reflects the initial atomic populations, as well as their subsequent SE redistribution predicted

<sup>\*</sup>christopher.kiehl@colorado.edu

<sup>&</sup>lt;sup>†</sup>Present address: Zurich Instruments AG, Technoparkstrasse 1, 8005 Zurich, Switzerland.

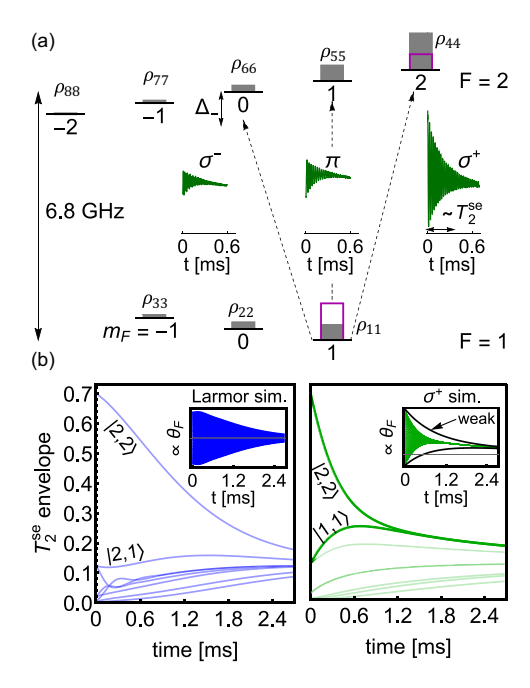


FIG. 1. (a) Energy-level diagram for <sup>87</sup>Rb showing the relevant microwave transitions and Rabi oscillations driving atomic populations ( $\rho_{ii}$ ) measured in our apparatus (green insets). A microwave sweep performs adiabatic rapid passage (ARP) to switch the  $\sigma^+$  populations prior to driving the  $\sigma^-$  and  $\pi$  transitions (magenta). (b) The envelopes of simulated atomic population dynamics due purely to SE collisions during Larmor precession (left) which decays slower than during a  $\sigma^+$  Rabi oscillation (right). Comparison of the envelopes for each state population to the full-simulated Faraday rotation signal (insets) shows nuanced population dynamics that are easier to individually observe with Rabi oscillations that couple a pair of states. The initial populations and SE rate here are set by a ST distribution with polarization p = 0.7 and vapor temperature  $T_v = 110\,^{\circ}\text{C}$ .

from our model. While similar population dynamics occurs with OPMs that sense the free Lamor precession, such SE effects are more apparent and distinguishable with Rabi oscillations that probe discrete states [Fig. 1(b)].

We first describe our theoretical model for driving Rabi oscillations in an alkali vapor cell. The relevant atomic dynamics occurs in the two hyperfine ground manifolds  $F = I \pm 1/2$ . Hence we describe the state of the atomic ensemble by a  $(4I + 2) \times (4I + 2)$  density matrix in the  $|F, m_F\rangle$  basis. The time evolution of the atomic ensemble including multiple sources of collisional decoherence is given by [19,20]

$$\begin{split} \frac{d\rho}{dt} &= \frac{[H(t), \rho]}{i\hbar} + \Gamma_{\rm se}(\phi(1 + 4\langle \mathbf{S} \rangle \cdot \mathbf{S}) - \rho) \\ &+ \Gamma_{\rm sd}(\phi - \rho) - \frac{\eta_I^2[I]}{8} \Gamma_{\rm C} \rho^{(\rm m)} + \Gamma_{\rm D}(\rho^e - \rho), \end{split} \tag{1}$$

where  $\phi = \rho/4 + \mathbf{S} \cdot \rho \mathbf{S}$  is known as the nuclear part of the density matrix for which  $\text{Tr}[\phi \mathbf{S}] = 0$  and  $\text{Tr}[\phi] = 1$  hold [22]. The Hamiltonian

$$H(t) = A_{\text{hfs}} \mathbf{I} \cdot \mathbf{S} + \mu_B (g_s \mathbf{S} + g_I \mathbf{I}) \cdot (B^{\text{dc}} \hat{\mathbf{z}} + \mathcal{B}^{\mu w}(t))$$
 (2)

describes the hyperfine structure, Zeeman shift from an applied dc magnetic field oriented along  $\hat{z}$ , and the

TABLE I. Cross sections, diffusion constant, and the corresponding collision rates  $\Gamma$  for the different collisional processes for a vapor cell with volume (3 × 3 × 2 mm³), vapor temperature  $\mathcal{T}_v = 107\,^{\circ}\text{C}$ , buffer gas pressure  $P_{\text{N}_2} = 180$  Torr (24 kPa), and diffusion constant  $D_0 = 0.221$  cm² s<sup>-1</sup> for Rb-N<sub>2</sub> buffer gas collisions scaled to our vapor temperature [26].

Collision	$\sigma \ (10^{-18} \ \mathrm{m^2})$	$\Gamma = n\sigma v^r \text{ (Hz)}$
(Rb-Rb) <sub>se</sub>	1.9 [27]	$6.2 \times 10^{3}$
$(Rb-Rb)_{sd}$	$1.77 \times 10^{-4}$ [28]	5.8
$(N_2-Rb)_{sd}$	$1.44 \times 10^{-8}$ [29]	41
$(N_2-Rb)_{Carver}$	$\Gamma_{\rm C}/[{\rm N}_2] = 394~{\rm amg}^{-1}~{\rm s}^{-1}~[23]$	$\Gamma_{\rm C} = 67$
Wall	$D_0 P_0 = 0.017 \text{ m}^2 \text{ Torr } [26]$	$\Gamma_D = 4.4 \times 10^2$

atom-microwave coupling [21]. Coherence effects due to SE and S-damping (SD) collisions that only affect the electron spin are modeled by the second and third terms of Eq. (1) [22]. Collision rates  $\Gamma_{\text{se(sd)}} \equiv n_a \sigma_{\text{se(sd)}} v^r$  are characterized by cross sections  $\sigma_{se(sd)}$ , the mean relative velocity of the colliding pair  $v^r$ , and  $n_a$   $(n_{\rm N_2})$  the atomic density for alkali (buffer gas) collisions [20]. The fourth term models pure dephasing of microwave transitions due to buffer gas collisions where  $\rho^{(m)}$ represents the density matrix with only off-diagonal terms of the coherences between the upper and lower hyperfine manifolds,  $\Gamma_{\rm C}$  is the Carver rate, and  $\eta_I = \mu_I/2I\mu_{\rm N}$  is the isotope coefficient [23,24]. The final term models diffusion into the cell walls where alkali spins are completely randomized [21]. Here,  $\rho^e$  is the equilibrium density matrix with all populations  $\rho_{ii}^e$  equal and  $\Gamma_D = D\pi^2/(l_x^2 + l_y^2 + l_z^2)$  is the fundamental decay mode defined by the vapor-cell dimensions  $l_x$ ,  $l_y$ , and  $l_z$  [25]. The diffusion constant  $D = D_0 P_0 / P_{N_2}$  is attenuated by the buffer gas pressure where  $P_0 = 1$  atm. For context, Table I contains the collision rates, cross sections, and diffusion constant assuming the vapor-cell parameters and the Rb-N<sub>2</sub> alkali-buffer gas mixture used in our experiment.

For hyperfine transitions, the SE dephasing rate  $\gamma_{\rm se} \equiv 1/T_2^{\rm se}$  is proportional to the collision rate  $\Gamma_{\rm se}$  and further depends on the atomic populations  $\rho_{ii}(t)$  due to the different projections of the  $|F,m_F\rangle$  basis on the electron spin. The weak-driving approximation  $\gamma_{\rm se}^{\rm wk}$  assumes fixed atomic populations which for the  $\sigma^+$  transition is given by [21]

$$\gamma_{\text{se}}^{\text{wk}} = \Gamma_{\text{se}} \left[ \frac{7}{8} (\rho_{44} - 1) + \frac{\rho_{11}}{2} + \frac{\rho_{33} - \rho_{77}}{16} + \frac{\rho_{55}}{4} - \frac{\rho_{88}}{8} \right].$$
(3)

For highly polarized ensembles with the majority of the atomic population in the "stretched" state  $|2,2\rangle$  nearly all of the electron spins are aligned so that no hyperfine-changing collisions occur due to spin exchange and consequently  $\gamma_{\rm se}^{\rm wk} \to 0$ . In contrast, SE collisions cause spin flips when there is population in states such as  $|1,1\rangle$  that have projections onto oppositely aligned electron spins. Therefore, strong population dynamics during Rabi oscillations implies a nontrivial coherence  $\gamma_{\rm se}$  and population redistribution beyond the weak driving approximation [Fig. 1(b)] that requires numerically solving Eq. (1) to accurately model.

To validate this theoretical description, we experimentally drive Rabi oscillations on the  $\sigma^{\pm}$  and  $\pi$  microwave transitions [Fig. 1(a)] near resonance where the theoretical

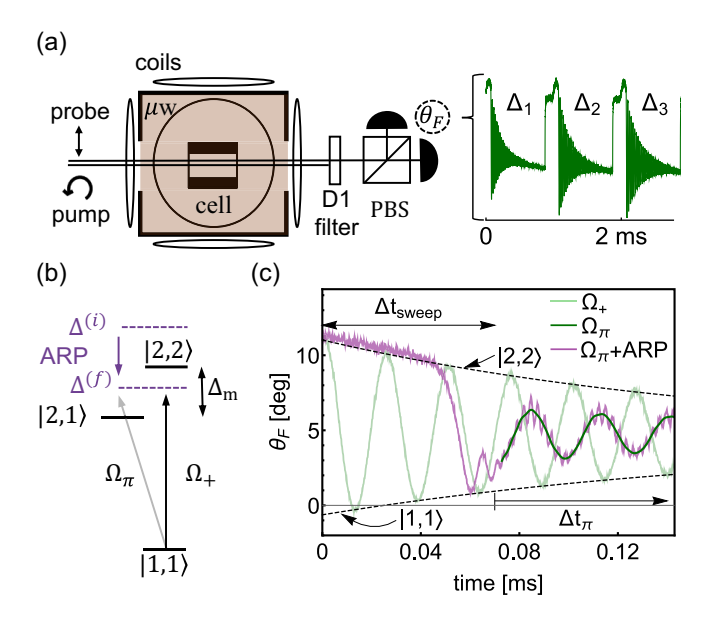


FIG. 2. (a) Apparatus for driving Rabi oscillations. We drive and measure Rabi oscillations between hyperfine states  $|1,1\rangle$  to  $|2,0\rangle$ ,  $|2,1\rangle$ , and  $|2,2\rangle$  at multiple detunings in real time using Faraday rotation readout of the macroscopic atomic spin state. (b) Energy-level diagram for adiabatic rapid passage (ARP). (c) Using ARP to maximize the  $|1,1\rangle$  population and enhance the  $\Omega_{\pi}$  signal. Overlaying with  $\Omega_{+}$  (light green) denotes  $\theta_{F}$  values for  $|2,2\rangle$  and  $|1,1\rangle$  occupation, where we observe ARP transfer (purple) after the microwave frequency sweep. Extracting the pure  $\pi$  oscillation (dark green) requires filtering off-resonance driving of adjacent transitions.

model predicts larger SE dephasing rates than the weakdriving approximation. Our apparatus [Fig. 2(a)] consists of a square-shaped  $(4.8 \times 4.8 \times 2 \text{ cm}^3)$  microwave cavity with the degenerate modes  $(n_x, n_y, n_z) = (2, 1, 0)$  and (1,2,0) tuned near the <sup>87</sup>Rb hyperfine ground state resonance (6.834 GHz), a microfabricated vapor cell ( $3 \times 3 \times 2 \text{ mm}^3$ ) filled with <sup>87</sup>Rb and  $P_{\rm N_2} \approx 180$  Torr (24 kPa) buffer gas, and a dc coil system consisting of three pairs of near-orthogonal coils to create a static magnetic field ( $\approx$ 50  $\mu$ T) to lift the degeneracy between adjacent magnetic sublevels by  $\Delta_m \approx 350$  kHz [Fig. 2(b)]. While the use of a cavity is not crucial for this investigation, we plan to exploit the cavity modes and the Rabi spectroscopy presented here for future control of microwave polarization for vector magnetometry [14]. Flexible polyimide heaters heat the microwave cavity, and by design, also the cell to near 107 °C. To avoid stray magnetic fields, we turn off the heaters 80 ms before each measurement. Due to the polarization structure of the microwave field, we tilt the magnetic field from the pump-beam axis by 25° such that a nonzero microwave field component drives all microwave hyperfine transitions with respect to  $|1, 1\rangle$  [Fig. 1(a)].

To study coherent population transfer, we infer the atomic state by measuring the Faraday rotation angle  $(\theta_F)$  of the probe beam  $\approx 80$  GHz detuned from the  $D_2$  line (780 nm) to obtain fast continuous measurements while minimizing decoherence from scattered light. While OPMs also typically use Faraday rotation to sense Larmor precession [20,30,31], all previous measurements of Rabi oscillations in vapor cells, to our knowledge, have used absorptive imaging to sense spin

dynamics [11,13,32,33]. Our readout enables measurements of consecutive Rabi oscillations for various microwave detunings  $(\Delta_1, \Delta_2, ...)$  and transitions in real time [Fig. 2(a)].

In each measurement, we first prepare a spin-polarized atomic ensemble by continuously optically pumping with circularly polarized light that is near-resonant with the  $D_1$ line (795 nm) for 100 µs. Immediately after, we adiabatically turn off the pumping light over the next 100 us to align the atomic spins with the static magnetic field and avoid Larmor precession. After preparation of the macroscopic atomic spin in the  $|2, 2\rangle$  state, we prepare the ensemble in the  $|1, 1\rangle$  state using adiabatic rapid passage (ARP) [Figs. 2(b) and 2(c)]. For this we switch on a strong microwave drive at detuning  $\Delta^{(i)}=490~\mathrm{kHz}$  above the  $\sigma^+$  resonance and then linearly chirp it to  $\Delta^{(f)} = -150$  kHz below the  $\sigma^+$  resonance within  $\Delta t_{\rm sweep} = 70 \,\mu \text{s}$ . Then, we continue to study the dynamics of Rabi oscillations by tuning the microwave drive to the hyperfine transition resonance. In the acquired data, we filter out high-frequency oscillations due to off-resonant coupling to adjacent microwave transitions [Fig. 2(c)]. Note, to study the  $\sigma^+$  transition that couples  $|1,1\rangle$  to  $|2,2\rangle$ , we do not perform an ARP.

To assess the accuracy of the theoretical model, we mimic the experimental sequence and parameters when solving Eq. (1) to compare the theoretical and measured dephasing rates and Rabi envelopes for the  $\sigma^{\pm}$  and  $\pi$  transitions as shown in Figs. 3(a) and 3(b). During this process we fit free parameters in our model that represent the vapor temperature  $\mathcal{T}_v$ , buffer gas pressure  $P_{\rm N_2}$ , and the electron spin polarization p produced by optical pumping, whose extracted values are consistent with independent knowledge of the apparatus. For modeling state preparation, we use the Rabi measurements to fit the atomic populations in each  $|F, m_F\rangle$  ground state  $\rho_{ii}^{\rm OP}$  subsequent to optical pumping and  $\rho_{ii}^{\rm ARP}$  produced after ARP. We find unique solutions for the atomic populations while also fixing the electron spin polarization p [21].

After spin preparation, we model the full atomic spin dynamics by solving Eq. (1) that provides  $\langle \mathcal{F}(t) \rangle$ , where  $\mathcal{F} = F_{z,b} - F_{z,a}$  is the difference between the z component of the hyperfine spin  $F_z$  in the b = I + 1/2 and a = I - 1/2manifolds. We model Faraday rotation by  $a_0 + b_0 \langle \mathcal{F}(t) \rangle =$  $\theta_F^{\text{sim}}(t)$ , where  $a_0$  is a scaling constant that we fit originating from the light-atom coupling and  $b_0$  is a measured initial polarization offset of the probe beam [21]. To account for higher-order diffusion modes affecting the wall-collision rate and residual light scattering from the probe, we independently measure the nonexponential dependence of macroscopic spin decay and model as an effective time-dependent wall collision rate  $\Gamma_{\rm D}(t)$ . We use fitted values 49.63  $\mu \rm T$  for the static magnetic field, 87.22 kHz for the hyperfine frequency shift from buffer gas collisions, and  $\{\Omega_-, \Omega_\pi, \Omega_+\} =$ {54.57, 35.03, 39.55} kHz extracted from Rabi oscillations driven at multiple detunings [21].

Our model extracts  $\mathcal{T}_v = 107\,^{\circ}\text{C}$ ,  $P_{\text{N}_2} = 190\,\text{Torr}$ , and  $p = 0.79\,$  from the measurements by utilizing all three Rabi line shapes to minimize the root-mean-square error (RMSE) between the simulated  $\theta_F^{\text{sim}}$  and the measured  $\theta_F$  [21]. The inset of Fig. 3(b) displays the RMSE over variations of the vapor temperature  $\mathcal{T}_v$  and the buffer gas pressure  $P_{\text{N}_2}$ , where the green circle marks the optimal values. The dephasing rates

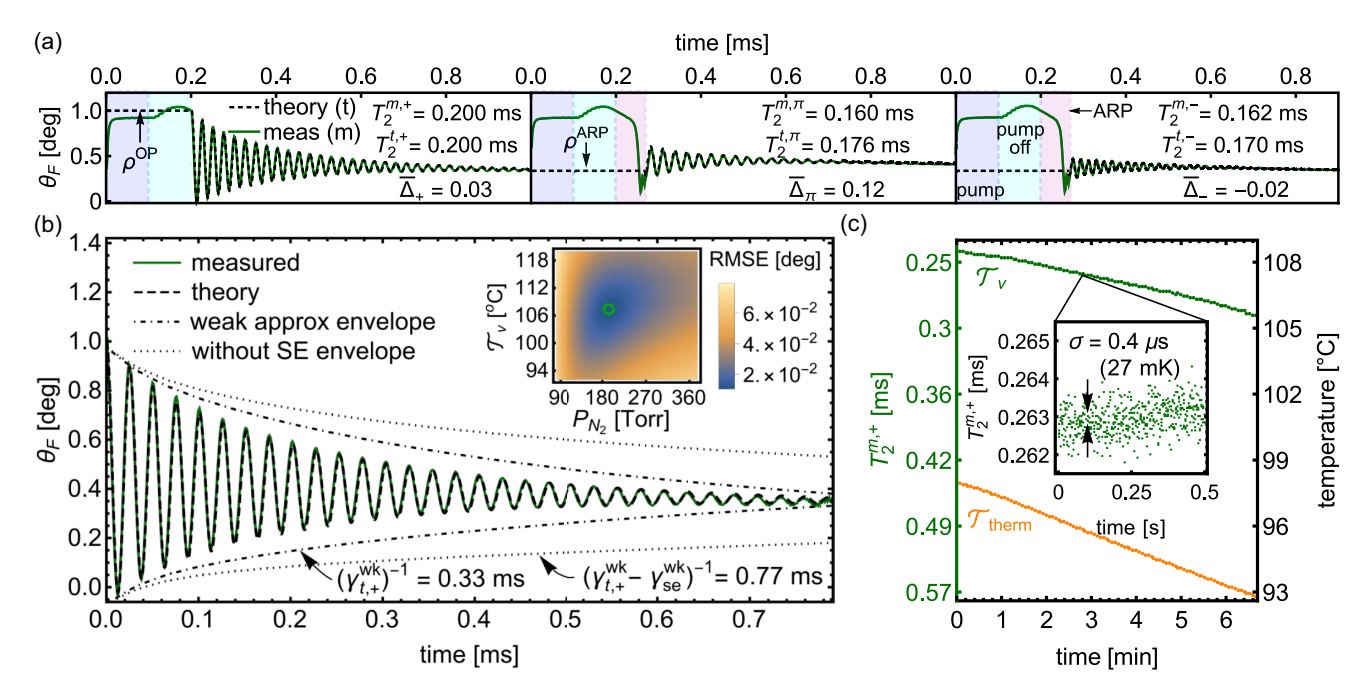


FIG. 3. (a) A mirror comparison of the simulated (black dashed) and measured (green)  $\sigma^+$ ,  $\pi$ , and  $\sigma^-$  Rabi oscillations. Here,  $\overline{\Delta}_{\pm,\pi} = \Delta_{\pm,\pi}/\Omega_{\pm,\pi}$  is the normalized microwave detuning. (b) A plot of the  $\sigma^+$  Rabi oscillation alongside other relevant decay rates. Importantly, the weak-driving approximation predicts much higher coherence compared to our measurements. The inset shows the RMSE between the simulated and measured Rabi oscillations for different vapor temperatures  $\mathcal{T}_v$  and buffer gas pressures  $P_{\rm N_2}$  at a fixed spin polarization p=0.79. By finding these optimal values where the theory and measured Rabi oscillations highly overlap, our model estimates these parameters for our cell. (c) Intracell thermometry with SE coherence measurements. The intracell temperature  $\mathcal{T}_v$  is inferred from measured dephasing times  $T_2^{m,+}$  using the calibrated model. The inset displays  $T_2^{m,+}$  fluctuations over a 0.5 s period.

 $\gamma_{t,j} = 1/T_2^{t,j}$  and nuanced features of the line shapes predicted theoretically agree with the measured dephasing times  $\gamma_{m,j} = 1/T_2^{m,j}$  and line shapes (black/green lines in Fig. 3). In contrast, the corresponding weak-driving approximation predicts a total dephasing time  $\gamma_{t,+}^{\text{wk}}$  for the  $\sigma^+$  Rabi oscillation that underestimates  $\gamma_{m,+}$  [Fig. 3(b)]. Here,  $\gamma_{t,+}^{\text{wk}}$  is extracted from fitting a single decay rate to a theoretical Rabi oscillation given by an exponentially decaying sine with instantaneous decay rate  $\gamma_{\rm se}^{\rm wk} + \gamma_{\rm sd} + \gamma_{\rm C} + \Gamma_{\rm D}(t)$  accounting for all sources of collisional decoherence but using the weak-driving approximation for the spin-exchange dephasing rate. In fact, in order for  $\gamma_{t,+}^{\text{wk}}$  to match the measured Rabi coherence would require  $T_v \rightarrow 122$  °C to sufficiently increase the SE collision rate. This is far from the thermistor temperature  $\mathcal{T}_{\text{therm}} = 98 \,^{\circ}\text{C}$ , which we expect is cooler than the vapor temperature  $\mathcal{T}_{v}$  by only a few °C due to thermal gradients across the microwave cavity. Furthermore, an electron spin polarization of p = 0.79is reasonable given the uncoated glass walls of our cell and the misalignment between the pump beam and the static magnetic field, and  $P_{\rm N_2} = 190$  Torr (25.3 kPa) is in close agreement with buffer gas pressures {170, 180, 330} Torr extracted independently from broadening and frequency shifts in both microwave and optical measurements [21].

Finally, we demonstrate the application of Rabi coherence to intracell thermometry [Fig. 3(c)], which is generally useful for characterizing the performance of atomic vapor sensing platforms and is particularly useful for stabilizing and optimizing the accuracy of atomic clocks [34,35]. In contrast, external sensors such as thermistors do not sense

the actual vapor temperature. Here, we cool the vapor cell by switching off the heat tape attached to the microwave cavity. While the cell cools, we record the Rabi dephasing time  $T_2^{m,+}$  by generating a 0.5-s-long train of 500  $\sigma^+$  Rabi oscillations triggered every 4 s over a 7-min cooling period of 3.5 °C. We map the measured dephasing time  $T_2^{m,+} \to \mathcal{T}_v$  to the intracell vapor temperature by varying  $\mathcal{T}_v$  within the calibrated theoretical model and fitting an interpolating polynomial  $\mathcal{P}$  to the simulated dephasing time  $\mathcal{T}_v = \mathcal{P}(T_2^{t,+})$ . The temperature dependence of  $1/T_2^{m,+} \propto n_{\rm Rb}\sigma_{\rm se}v^r$  arises from the atomic density, which decreases as the vapor cell cools. From a single 500-ms train of Rabi oscillations we measure a temperature sensitivity of 1.2 mK/ $\sqrt{\rm Hz}$  [Fig. 3(c) inset]. This is a competitive sensitivity with other techniques [34,36], and demonstrates Rabi coherence as a novel platform for intracell thermometry.

In conclusion, this work completes previous investigations of hyperfine coherence by using an exact numerical model and continuous QND sensing in a vapor cell to study significant deviations of SE coherence from the weak-driving predictions assumed historically. In contrast to configurations with static atomic populations, Rabi oscillations between hyperfine manifolds in heated vapor cells exhibit nontrivial atomic dynamics due to SE effects, which prevents accurate evaluation and understanding of sensitivities for the increasing applications of Rabi oscillations in metrology applications. We find excellent agreement with the coherence predicted by our model and Rabi oscillation measurements. Moreover, we find further agreement with the fact that we can exploit

multiple hyperfine transitions to determine vapor-cell parameters and temperature dependence that are consistent with independent characterizations. This extended information that harnesses SE effects may be useful for vapor-cell characterization and intracell thermometry in future experiments and the continuous Rabi measurements presented here will be an important component of working toward a use in absolute vector magnetometry [14].

This work was supported by DARPA through ARO Grants No. W911NF-19-1-0330 and No. W911NF-21-1-0127, NSF QLCI Award No. OMA - 2016244, ONR Grant No. N00014-17-1-2245, and NSF Grant No. PHYS 1734006. We acknowledge helpful conversations with Y.-Y. Jau, C. Affolderbach, V. Gerginov, and M. Ellmeier, and technical expertise from T. S. Menon, Y. Duerst, and F. Vietmeyer.

- [1] J. Vanier and C. Audoin, *The Quantum Physics of Atomic Frequency Standards* (A. Hilger, Bristol, UK, 1989), Vol 1.
- [2] W. Happer, Optical Pumping, Rev. Mod. Phys. 44, 169 (1972).
- [3] J. Kong. R. Jiménez-Martínez, C. Troullinou, V. G. Lucivero, G. Tóth, and M. W. Mitchell, Measurement-induced, spatiallyextended entanglement in a hot, strongly-interacting atomic system, Nat. Commun. 11, 2415 (2020).
- [4] Y. Horowicz, O. Katz, O. Raz, and O. Firstenberg, Critical dynamics and phase transition of a strongly interacting warm spin gas, Proc. Natl. Acad. Sci. USA 118, e2106400118 (2021).
- [5] D. Budker and M. Romalis, Optical magnetometry, Nat. Phys. 3, 227 (2007).
- [6] W. Happer and H. Tang, Spin-Exchange Shift and Narrowing of Magnetic Resonance Lines in Optically Pumped Alkali Vapors, Phys. Rev. Lett. 31, 273 (1973).
- [7] I. M. Savukov and M. V. Romalis, Effects of spin-exchange collisions in a high-density alkali-metal vapor in low magnetic fields, Phys. Rev. A 71, 023405 (2005).
- [8] J. Vanier, Relaxation in Rubidium-87 and the Rubidium Maser, Phys. Rev. 168, 129 (1968).
- [9] J. Vanier, J.-F. Simard, and J.-S. Boulanger, Relaxation and frequency shifts in the ground state of Rb<sup>85</sup>, Phys. Rev. A 9, 1031 (1974).
- [10] Y.-Y. Jau, A. B. Post, N. N. Kuzma, A. M. Braun, M. V. Romalis, and W. Happer, Intense, Narrow Atomic-Clock Resonances, Phys. Rev. Lett. 92, 110801 (2004).
- [11] A. Horsley, G.-X. Du, and P. Treutlein, Widefield microwave imaging in alkali vapor cells with sub-100 μm resolution, New J. Phys. 17, 112002 (2015).
- [12] A. Horsley and P. Treutlein, Frequency-tunable microwave field detection in an atomic vapor cell, Appl. Phys. Lett. 108, 211102 (2016).
- [13] P. Böhi and P. Treutlein, Simple microwave field imaging technique using hot atomic vapor cells, Appl. Phys. Lett. **101**, 181107 (2012).
- [14] T. Thiele, Y. Lin, M. O. Brown, and C. A. Regal, Self-Calibrating Vector Atomic Magnetometry through Microwave Polarization Reconstruction, Phys. Rev. Lett. 121, 153202 (2018).
- [15] E. C. Fear, S. C. Hagness, P. M. Meaney, M. Okoniewski, and M. A. Stuchly, Enhancing breast tumor detection with near-field imaging, IEEE Microwave Mag. 3, 48 (2002).
- [16] N. K. Nikolova, Microwave imaging for breast cancer, IEEE Microwave Mag. 12, 78 (2011).
- [17] R. Chandra, H. Zhou, I. Balasingham, and R. M. Narayanan, On the opportunities and challenges in microwave medical sensing and imaging, IEEE Trans. Biomed. Eng. **62**, 1667 (2015).

- [18] J. P. Wittke and R. Dicke, Redetermination of the Hyperfine Splitting in the Ground State of Atomic Hydrogen, Phys. Rev. **103**, 620 (1956).
- [19] D. Budker and D. F. J. Kimball, Optical Magnetometry (Cambridge University Press, Oxford, UK, 2013).
- [20] J. C. Allred, R. N. Lyman, T. W. Kornack, and M. V. Romalis, High-Sensitivity Atomic Magnetometer Unaffected by Spin-Exchange Relaxation, Phys. Rev. Lett. 89, 130801 (2002).
- [21] See Supplemental Material at http://link.aps.org/supplemental/ 10.1103/PhysRevResearch.5.L012002 for details on the atommicrowave coupled Hamiltonian, atomic collisions, experiment modeling, and independent measurements of buffer-gas pressure.
- [22] S. Appelt, A. B. Baranga, C. J. Erickson, M. V. Romalis, A. R. Young, and W. Happer, Theory of spin-exchange optical pumping of <sup>3</sup>He and <sup>129</sup>Xe, Phys. Rev. A **58**, 1412 (1998).
- [23] D. K. Walter, W. M. Griffith, and W. Happer, Magnetic Slowing Down of Spin Relaxation due to Binary Collisions of Alkali-Metal Atoms with Buffer-Gas Atoms, Phys. Rev. Lett. 88, 093004 (2002).
- [24] Y.-Y. Jau, New studies of optical pumping, spin resonances, and spin exchange in mixtures of inert gases and alkali-metal vapors, Ph.D. thesis, Princeton University, 2005.
- [25] W. Franzen, Spin Relaxation of Optically Aligned Rubidium Vapor, Phys. Rev. 115, 850 (1959).
- [26] A. Pouliot, G. Carlse, H. C. Beica, T. Vacheresse, A. Kumarakrishnan, U. Shim, S. B. Cahn, A. Turlapov, and T. Sleator, Accurate determination of an alkali-vapor-inert-gas diffusion coefficient using coherent transient emission from a density grating, Phys. Rev. A 103, 023112 (2021).
- [27] S. Micalizio, A. Godone, F. Levi, and J. Vanier, Spin-exchange frequency shift in alkali-metal-vapor cell frequency standards, Phys. Rev. A **73**, 033414 (2006).
- [28] A. B.-A. Baranga, S. Appelt, M. Romalis, C. Erickson, A. Young, G. Cates, and W. Happer, Polarization of <sup>3</sup>He by Spin Exchange with Optically Pumped Rb and K Vapors, Phys. Rev. Lett. **80**, 2801 (1998).
- [29] M. E. Wagshul and T. Chupp, Optical pumping of high-density Rb with a broadband dye laser and GaAlAs diode laser arrays: Application to <sup>3</sup>He polarization, Phys. Rev. A **40**, 4447 (1989).
- [30] V. Shah, G. Vasilakis, and M. V. Romalis, High Bandwidth Atomic Magnetometery with Continuous Quantum Nondemolition Measurements, Phys. Rev. Lett. 104, 013601 (2010).
- [31] S. Li, P. Vachaspati, D. Sheng, N. Dural, and M. V. Romalis, Optical rotation in excess of 100 rad generated by Rb vapor in a multipass cell, Phys. Rev. A **84**, 061403(R) (2011).
- [32] C. Affordbach, G. X. Du, T. Bandi, A. Horsley, P. Treutlein, and G. Mileti, Imaging microwave and dc magnetic fields in

- a vapor-cell Rb atomic clock, IEEE Trans. Instrum. Meas. **64**, 3629 (2015).
- [33] G. Liu, O. Be'er, Y. Margalit, M. Givon, D. Groswasser, Y. Japha, and R. Folman, Survival of the fittest in the coherent evolution of quantum ensembles, Phys. Rev. A **98**, 013856 (2018).
- [34] N. P. Wells, T. U. Driskell, and J. C. Camparo, in 2014 European Frequency and Time Forum (EFTF) (IEEE, New York, 2014), pp. 548–553.
- [35] Q. Hao, W. Xue, F. Xu, K. Wang, P. Yun, and S. Zhang, Efforts towards a low-temperature-sensitive physics package for vapor cell atomic clocks, Satell. Navig. 1, 17 (2020).
- [36] M. Salleras, E. Eklund, I. Prikhodko, and A. Shkel, Predictive thermal model for indirect temperature measurement inside atomic cell of nuclear magnetic resonance gyroscope, in *TRANSDUCERS 2009 International Solid-State Sensors, Actuators and Microsystems Conference* (IEEE, New York, 2009), pp. 304–307.